Supporting Information for

Proof of Aerobically Autoxidized Self-Charge Concept Based on Single Catechol-Enriched Carbon Cathode Material

Junyan Wang[1], Wanchun Guo[1,*], Kesong Tian[1,*], Xinta Li[1], Xinyu Wang[1], Panhua Li[1], Yu Zhang[1], Bosen Zhang[1], Biao Zhang[2], Shuhu Liu[3], Xueai Li[1], Zhaopeng Xu[1], Junjie Xu[4], Haiyan Wang[1,*], Yanglong Hou[2,*]

[1] State Key Laboratory of Metastable Materials Science and Technology, Hebei Key Laboratory of Heavy Metal Deep-Remediation in Water and Resource Reuse, School of Environmental and Chemical Engineering, Yanshan University, 066004 Qinhuangdao, P. R. China

[2] Beijing Key Laboratory for Magnetoelectric Materials and Devices, Beijing Innovation Centre for Engineering Science and Advanced Technology, School of Materials Science and Engineering, Peking University, 100871 Beijing, P. R. China

[3] Institute of High Energy Physics, Chinese Academy of Sciences, 100049 Beijing, P. R. China

[4] Xi'an Rare Metal Materials Institute Co., Ltd, 710016 Xi'an, P. R. China

*Corresponding authors. E-mail: wc-g@ysu.edu.cn (Wanchun Guo); tiankesong@ysu.edu.cn (Kesong Tian); hywang@ysu.edu.cn (Haiyan Wang); hou@pku.edu.cn (Yanglong Hou)

Supplementary Figures

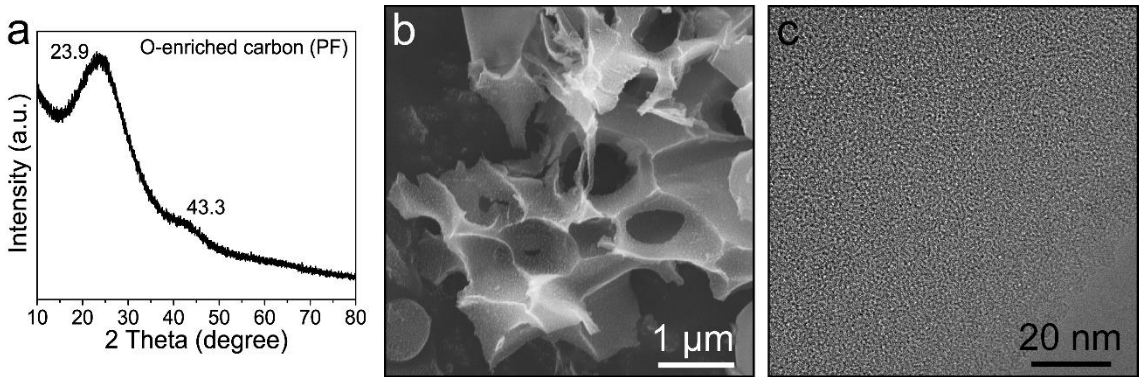

Fig. S1 Structural characterization of oxygen-enriched carbon (PF) material. **a** XRD pattern, **b** SEM, **c** HRTEM images

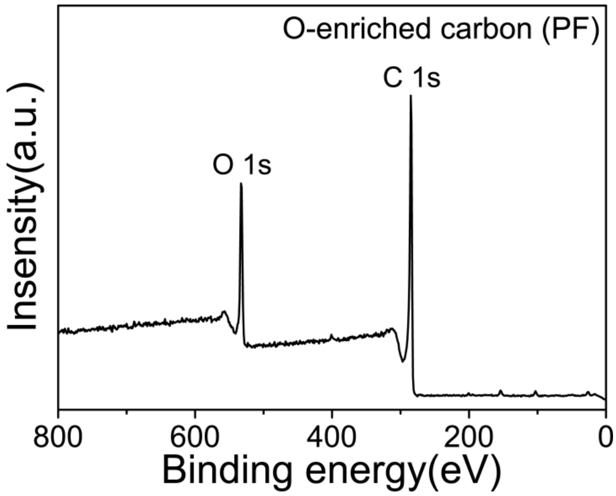

Fig. S2 XPS survey spectrum of oxygen-enriched carbon (PF) material

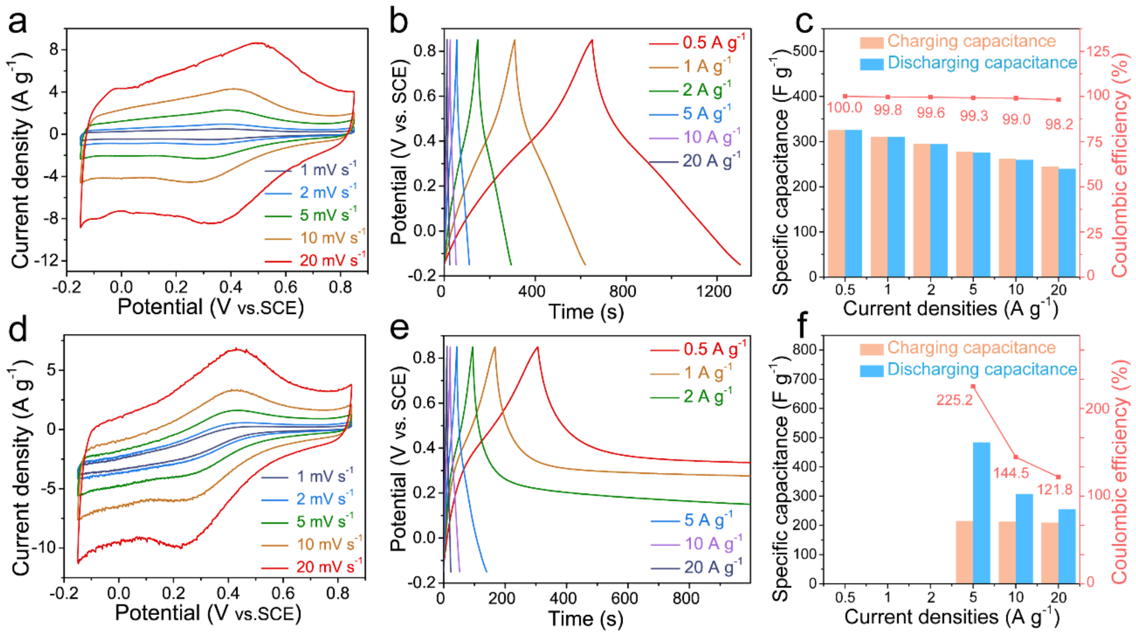

Fig. S3 Electrochemical performance evaluation of oxygen-enriched carbon (PF) material. **a** CV tests under saturated N_2 atmosphere. **b** Galvanostatic charge/discharge curves under saturated N_2 atmosphere. **c** The corresponding specific charge/discharge capacitance values and coulombic efficiency calculated through the GCD curves in Fig. S3b. **d** CV tests under saturated O_2 atmosphere. **e** Galvanostatic charge/discharge curves under saturated O_2 atmosphere. **f** The corresponding specific charge/discharge capacitance values and coulombic efficiency calculated through the GCD curves in Fig. S3e

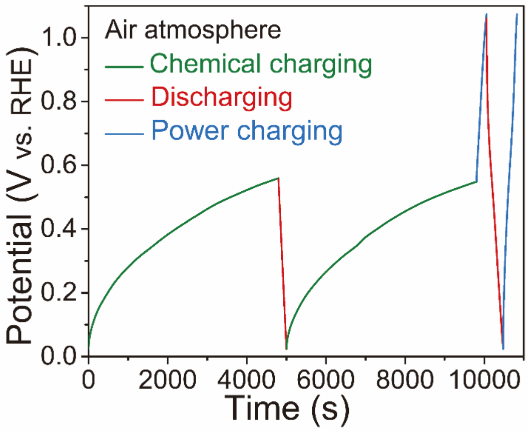

Fig. S4 Charge/discharge behavior of oxygen-enriched carbon (PF) material at chemical or/and galvanostatic charge hybrid modes in air atmosphere in a three-electrode system with 1 M H_2SO_4 aqueous solution

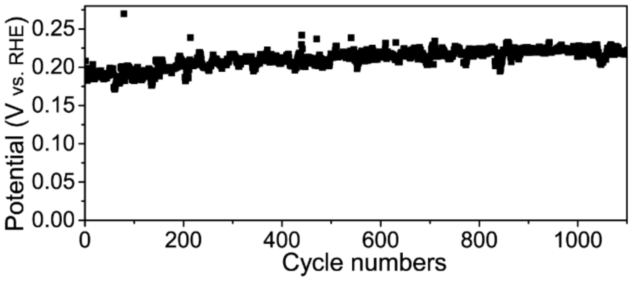

Fig. S5 Electrochemical stability of oxygen-enriched (PF) material. In every cycle, the oxygen-enriched carbon (PF) electrode was chemically charged at air atmosphere for 20 min to measure the potential and subsequently discharged at 1 A g^{-1} in a three-electrode system with 1 M H_2SO_4 aqueous solution as the electrolyte

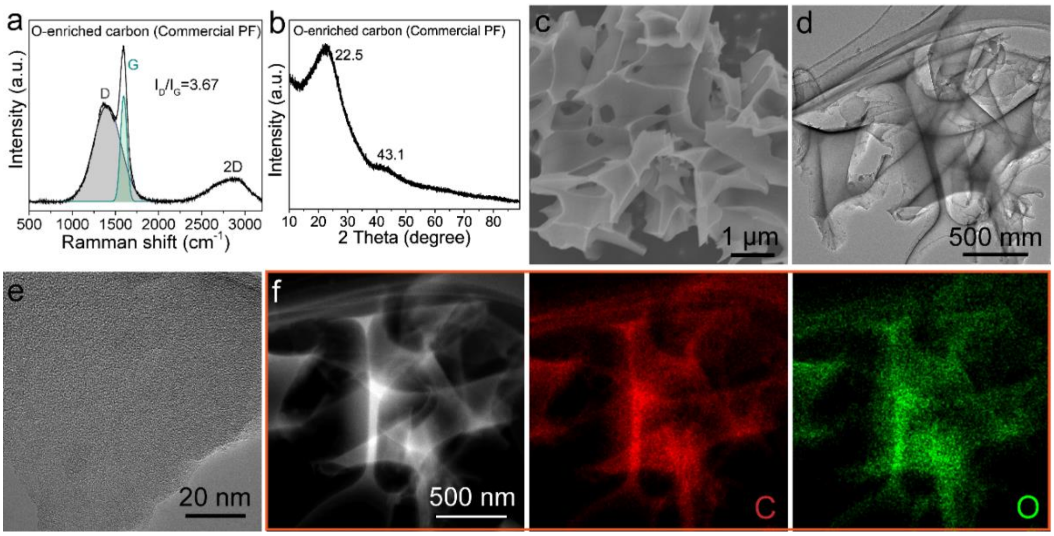

Fig. S6 Characterization of oxygen-enriched carbon (Commercial PF) material. **a** Raman spectrum. **b** XRD pattern. **c** SEM. **d** TEM. **e** HRTEM. **f** HADF-STEM images and the elemental mapping images of carbon and oxygen

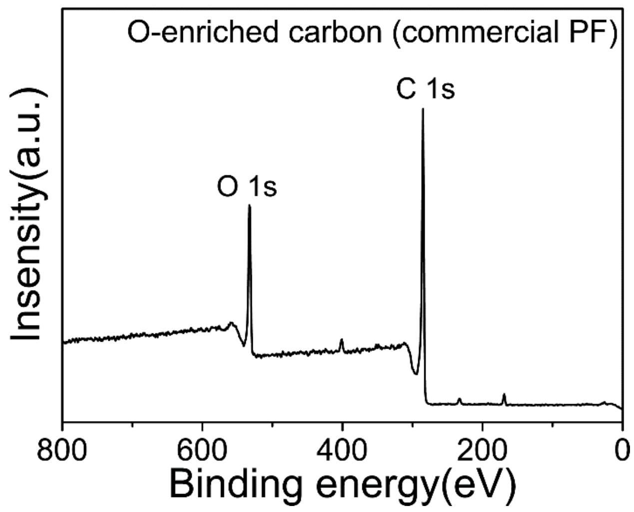

Fig. S7 XPS survey spectrum of oxygen-enriched carbon (Commercial PF) material

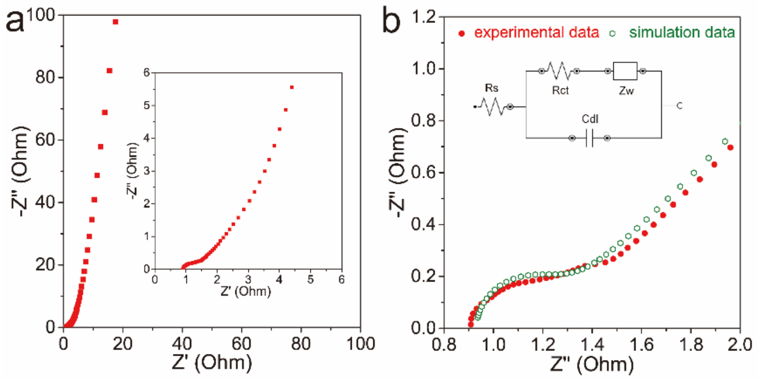

Fig. S8 Electrochemical impedance spectroscopy (EIS) for oxygen-enriched carbon (PF) cathode. **a** Complex-plane plots of EIS in frequency ranged from 0.01 to 100,000 Hz in 1.0 M H_2SO_4. The inset shows the corresponding details at high-frequency ranges. **b** Nyquist plots (red dots) and Nyquist plot simulation (green circles) of EIS. The inset

Table S1 Binding energies and FWHMs for O 1s XPS spectrum of oxygen-enriched carbon (PF) material in Fig. 2

Sample	-C=O B.E. (eV)	-C=O FWHM (eV)	-C-O B.E. (eV)	-C-O FWHM (eV)
O-enriched carbon (PF)	532.0	1.7	533.1	1.7

Table S2 The capacitance of air-breathing chargeable system of oxygen-enriched carbon (PF) material in three-electrode system at 1 A g^{-1} in 1.0 M H_2SO_4 electrolyte.

Oxidized time (min)	20	40	60	80	100	120
Capacitance (F g^{-1})	65	114	168	208	244	264

Table S3 Binding energies and FWHMs for O 1s XPS spectrum of oxygen-enriched carbon (PF) material in Fig. 3

Sample	-C=O B.E. (eV)	-C=O FWHM (eV)	-C-O B.E. (eV)	-C-O FWHM (eV)
Air-breathing charging for 2 h	532.0	1.8	533.2	1.7
Discharging in Saturated N_2	531.9	1.8	533.3	1.9

Table S4 Binding energies and FWHM for O 1s of oxygen-enriched carbon (Commercial PF) material in Fig. 4

Sample	-C=O B.E. (eV)	-C=O FWHM (eV)	-C-O B.E. (eV)	-C-O FWHM (eV)
O-enriched carbon (Commercial PF)	532.0	1.8	533.2	1.8

Table S5 The capacitance of air-breathing chargeable system of oxygen-enriched carbon (Commercial PF) material in three-electrode system at 1 A g^{-1} in 1.0 M H_2SO_4 electrolyte.

Oxidized time (min)	20	40	60	80	100	120
Capacitance (F g^{-1})	60	99	130	165	185	213

Supplementary Results and Discussion

Note S1 Electrochemical performance evaluation of oxygen-enriched carbon (PF) material in saturated N_2 and O_2

In order to elucidate the cause behind the coulombic efficiencies of oxygen-enriched carbon (PF) material in air higher than 100% at current densities from 0.5 to 20 A g^{-1}, electrochemical performances of the oxygen-enriched carbon (PF) electrode in 1 M H_2SO_4 solution in different atmospheres including saturated N_2 and O_2 were evaluated. (1) The CV curves of the oxygen-enriched carbon (PF) electrode in saturated N_2 at different scan rates (1-20 mV s^{-1}) with a pair of symmetrical peaks (0.3-0.4 V vs. SCE) (Fig. S3a) and the symmetrical GCD curves at various current densities with distorted linear shapes (Fig. S3b) in 1 M H_2SO_4 aqueous solution exhibited reversible Faraday redox reactions corresponding to the mutual conversion between catechol and *ortho*-quinone groups. Different from the coulombic efficiencies of oxygen-enriched carbon (PF) material at current densities from 0.5 to 20 A g^{-1} in air higher than 100%, those in saturated N_2 were equivalent to or slightly lower 100% (Fig. S3c). (2) The CV curves of the oxygen-enriched carbon (PF) electrode in saturated O_2 at different scan rates (1-20 mV s^{-1}) with a pair of symmetrical peaks (0.3-0.4 V vs. SCE) (Fig. S3d) in 1 M H_2SO_4 aqueous solution exhibited reversible Faraday redox reactions corresponding to the mutual conversion between catechol and *ortho*-quinone groups. According to GCD curves in saturated O_2 at various current densities from 0.5 to 20 A g^{-1} (Fig. S3e), the discharge capacitances were far higher than the corresponding charge capacitances; thus, the coulombic efficiencies were far higher than 100% at current densities from 0.5 to 20 A g^{-1} (Fig. S3f).

Note S2 Structural Characterization of oxygen-enriched carbon (Commercial PF) material

Raman spectrum of oxygen-enriched carbon (Commercial PF) material (Fig. S6a) shows a typical feature of sp^2-hybridized amorphous carbon materials with abundant defects, according to broad D band at 1398 cm^{-1} and G band at 1594 cm^{-1} corresponding to the breathing mode of the A1g symmetry and in-plane bond-stretching of sp^2 carbon atoms, respectively. Its X-ray diffraction (XRD) pattern (Fig. S6b) also provides another evidence of the characteristic of amorphous carbon materials with broadened (002) and (100)/(101) diffraction peaks at 22.5° and 43.1° analogous to the features of graphite. In addition, the scanning electron microscopy (SEM) (Fig. S6c), transmission electron microscopy (TEM) (Fig. S6d), and high-resolution transmission electron microscopy (HRTEM) (Fig. S6e) images further verify the amorphous feature of oxygen-enriched carbon (Commercial PF) material in the form of the nanosheet with the long-range disorder and local short-range order structure. Energy dispersive X-ray spectroscopy (EDS) elemental mapping images combined with HADF-STEM image (Fig. S6f) reveal a uniform distribution of oxygen species into carbon framework for oxygen-enriched carbon (Commercial PF) material. X-ray photoelectronic spectroscopy (XPS) survey spectrum of oxygen-enriched carbon (Commercial PF) material (Fig. S7) further verifies the existence of abundant oxygen species in carbon materials.